npj | computational materials

Article

Published in partnership with the Shanghai Institute of Ceramics of the Chinese Academy of Sciences

https://doi.org/10.1038/s41524-024-01233-6

Nonlinear dynamics of directly coupled skyrmions in ferrimagnetic spin torque nano-oscillators

Check for updates

Laichuan Shen [1,2,3], **Lei Qiu** [1,2,3] & **Ka Shen** [1,2] ✉

Nonlinear spin torque nano-oscillators have received substantial attentions due to their important applications in microwave communication and neuromorphic computing. Here we investigate the dynamical behaviors of directly coupled skyrmion oscillators in a synthetic ferrimagnet. We demonstrate through the micromagnetic simulation and Thiele's equation that the skyrmion oscillators can present either synchronization or frequency comb, depending on the strength of interactions between the skyrmions. The underlying physics of the transition between the two scenarios are unveiled based on a quantitative analysis of the effective potentials, which also successfully interprets the dependence of the transition on parameters. By further demonstrating the tunability of the nonlinear dynamics by the driving current of the oscillators, our work reveals the great potentials of ferrimagnetic-skyrmion-based interacting oscillators for nonlinear applications.

Nonlinear phenomena are of great interests and particularly useful for applications. One important example in spintronics is the spin torque nano-oscillator (STNO)[1–11], where the magnetic dissipation is fully compensated by the current-induced spin torque[12,13], exhibiting persistent oscillations of particular magnetic textures, such as uniform magnetization[1,14–16], magnetic vortices[2,3,17–20], skyrmions[7,21–23], etc. Potential applications of STNOs include microwave generators in communication technology and core elements in recently developed neuromorphic spintronics[24–29]. For a multi-STNO system, the interactions between different STNOs can give rise to additional intriguing nonlinear dynamics, for instance, the mutual synchronization, which corresponds to the situation where all STNOs oscillate with the same frequency and the same phase[30] so that the radiation power of the STNOs can be significantly enhanced, compared to an individual single-STNO-based microwave generator. Another interesting nonlinear phenomenon of interacting oscillators, the so-called frequency comb characterized by equally spaced discrete frequencies in the spectrum[31,32], has received increasing research attention[33–35] and been predicted also in magnetic systems[36–41].

Among the reported proposals, the synchronization and frequency comb based on spatially separated STNOs coupled through dipolar field require the fabrication of a patterned magnetic working layer[39], which might reduce the quality of the devices and cause additional cost. The weak strength of the dipolar-induced coupling not only limits the window of frequency mismatch between the oscillators, but also hinders the synchronization of multiple oscillators[42]. Those STNOs coupled through spin waves within one magnetic working layer[36–38], on the other hand, inevitably suffer from energy inefficiency due to the large dissipation in form of spin waves irrelevant to the coupling between the STNOs. Moreover, owing to the mutual disturbance of the dynamical magnetizations in the neighboring STNOs, there is a critical distance between the STNOs, below which neither the frequency comb nor the synchronization can be stabilized by the spin-wave-induced coupling[37], which hinders the device miniaturization for related applications. Recent theoretical proposal of individual boundary-free ferrimagnetic (FiM)-skyrmion-based STNO[43] sheds some light to overcome these problems and stimulates the present study.

In this work, we demonstrate theoretically both synchronization and frequency comb in the dynamics of two coupled FiM-skyrmion-based STNOs, where the repulsive coupling strength between skyrmions results from the instantaneous spatial overlap between their magnetic texture and therefore depends on not only the distance of the STNOs but also the trajectories of the skyrmion motion[44–46]. An explicit analysis on the interacting energy and the current-induced potential well interprets the condition of the transition between synchronization and frequency comb obtained from micromagnetic simulations. The extension of these nonlinear dynamical behaviors to a STNO array and their tunability by the applied currents are also demonstrated.

[1]The Center for Advanced Quantum Studies and Department of Physics, Beijing Normal University, 100875 Beijing, China. [2]Key Laboratory of Multi-scale Spin Physics, Ministry of Education, Beijing Normal University, 100875 Beijing, China. [3]These authors contributed equally: Laichuan Shen, Lei Qiu.
✉e-mail: kashen@bnu.edu.cn

Results and discussion

Theoretical model

Figure 1a depicts our model with two skyrmion-based STNOs, where the magnetic working layer is a synthetic ferrimagnetic (SFiM) film composed of two ferromagnets with different magnetizations (parameterized by $\mathbf{M}^{\mathrm{t}}$ and $\mathbf{M}^{\mathrm{b}}$), which are coupled by a relatively strong antiferromagnetic Ruderman–Kittel–Kasuya–Yosida (RKKY) interaction[47,48]. The skyrmion textures in the two ferromagnets are therefore bound together to behave as a single SFiM skyrmion (see Fig. 1b for the magnetic structure). Current injectors constructed by the spacer and fixed layer are placed on top of the SFiM film in order to generate spin transfer torques to trigger the SFiM-skyrmion dynamics, more explicitly, a stable orbital motion around the edge of each current injector[43] (see Fig. 1c).

To investigate the consequences of the dynamical interactions between the SFiM skyrmions, we employ the open-source micromagnetic software MUMAX3[49] to simulate the magnetization dynamics (see "Methods" section for the details). With the magnetic structure from micromagnetic simulations, we also evaluate the parameters in the phenomenological equation of skyrmion motion, i.e., the Thiele's equation[43,50–53], which could provide a comprehensive understanding of the coupled skyrmion dynamics. Specifically, as derived in Supplementary Note 1, the Thiele's equation of ith skyrmion can be written as

$$\mathbf{m}_{\mathrm{eff},i} \cdot \ddot{\mathbf{r}}_{\mathrm{c},i} = \mathbf{G}_i \times \dot{\mathbf{r}}_{\mathrm{c},i} - \alpha \mathbf{L}_i \cdot \dot{\mathbf{r}}_{\mathrm{c},i} + \mathbf{F}_{j,i} + \mathbf{F}_{\mathrm{ss},i}, \quad (1)$$

where $\mathbf{m}_{\mathrm{eff}}$ is the effective mass tensor, $\mathbf{G}$ the gyrovector, α the damping constant, and $\mathbf{L}$ the dissipative tensor. The instantaneous location $\mathbf{r}_{\mathrm{c}}$ of the SFiM skyrmion, with respect to the center of the corresponding current injector, is defined by its guiding center[54], as shown in Fig. 1c. $\mathbf{F}_j$ and $\mathbf{F}_{\mathrm{ss}}$ correspond to the current-induced force and the one from skyrmion-skyrmion interaction, respectively. More details of Eq. (1) are presented in Supplementary Note 1.

Synchronization and frequency comb

We consider different values of the injected currents through the two STNOs to drive them with a small free-running frequency difference. The dynamic properties of the two STNOs are read out by the local magnetizations averaged over the detection areas (Area1 and Area2 in Fig. 1a), $m^{\mathrm{t}}_{x,\mathrm{A}_1}$ and $m^{\mathrm{t}}_{x,\mathrm{A}_2}$, which reflect the output signals in magnetoresistance measurement. The micromagnetic simulation with different values of oscillator spacing (d_{12}) shows distinct dynamic properties. Specifically, when the spacing is too large, as shown by Fig. 1d with $d_{12} = 70$ nm, the two STNOs simply present individual oscillations. At a moderate spacing, they interfere with each other, resulting in a nice frequency comb (see Fig. 1e with $d_{12} = 50$ nm). Once d_{12} becomes sufficiently small, the oscillations of the two STNOs are forced to share a common frequency, corresponding to a synchronization (Fig. 1f with $d_{12} = 40$ nm). Supplementary Movies 1 and 2 show the dynamic behavior of skyrmions in frequency comb and synchronization situations, respectively.

To gain a deeper understanding of the evolution of the above dynamics with varying d_{12}, the trajectories of the skyrmion motion, which are responsible for the time-dependent $m^{\mathrm{t}}_{x,\mathrm{A}_i}$, are calculated from both the MUMAX3 and Thiele's equation and presented in Supplementary Fig. 2 with different values of d_{12}. Accordingly, FFT spectra of the x components of the skyrmion locations, $r_{\mathrm{c}x,1}$ and $r_{\mathrm{c}x,2}$, are plotted in Fig. 2, which exhibits exactly the same frequency characteristics as those in Fig. 1. Namely, before entering the synchronization situation, the FFT spectrum experiences a frequency comb due to nonlinear effects[55]. The equal spacing in the frequency comb scenario can be clearly recognized in Fig. 2c, d with $d_{12} = 50$ nm. As seen, the results from the Thiele's

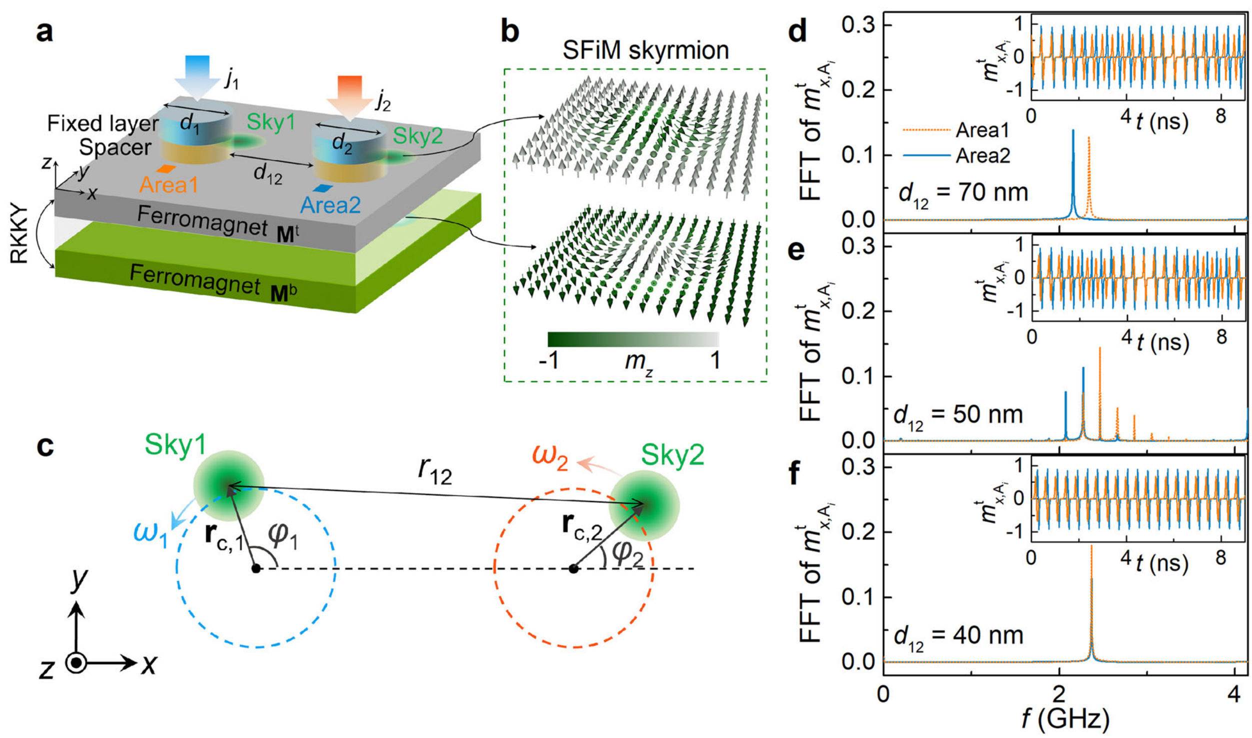

Fig. 1 | Nonlinear dynamics in coupled SFiM-skyrmion-based STNOs. a Sketch of two coupled skyrmion-based STNOs. **b** Magnetic texture of the SFiM skyrmion. The color bar represents the z component of magnetization. **c** Definitions of the quantities to describe the rotational motion of the skyrmions. The blue and orange dashed circles indicate the current injection areas. **d**–**f** Fast Fourier transformation (FFT) spectra of the recorded magnetizations $m^{\mathrm{t}}_{x,\mathrm{A}_1}$ and $m^{\mathrm{t}}_{x,\mathrm{A}_2}$ averaged separately over Area1 and Area2 indicated in **a**, with oscillator spacing $d_{12} = 70$, 50 and 40 nm. The insets show the time evolution of magnetizations. In the calculation, we take the diameters of the circular injectors $d_1 = d_2 = 30$ nm, saturation magnetizations $M^{\mathrm{t}}_{\mathrm{s}} = 600\ \mathrm{kA\ m^{-1}}$ and $M^{\mathrm{b}}_{\mathrm{s}} = 580\ \mathrm{kA\ m^{-1}}$, and driving currents $j_1 = 40\ \mathrm{MA\ cm^{-2}}$ and $j_2 = 80\ \mathrm{MA\ cm^{-2}}$.

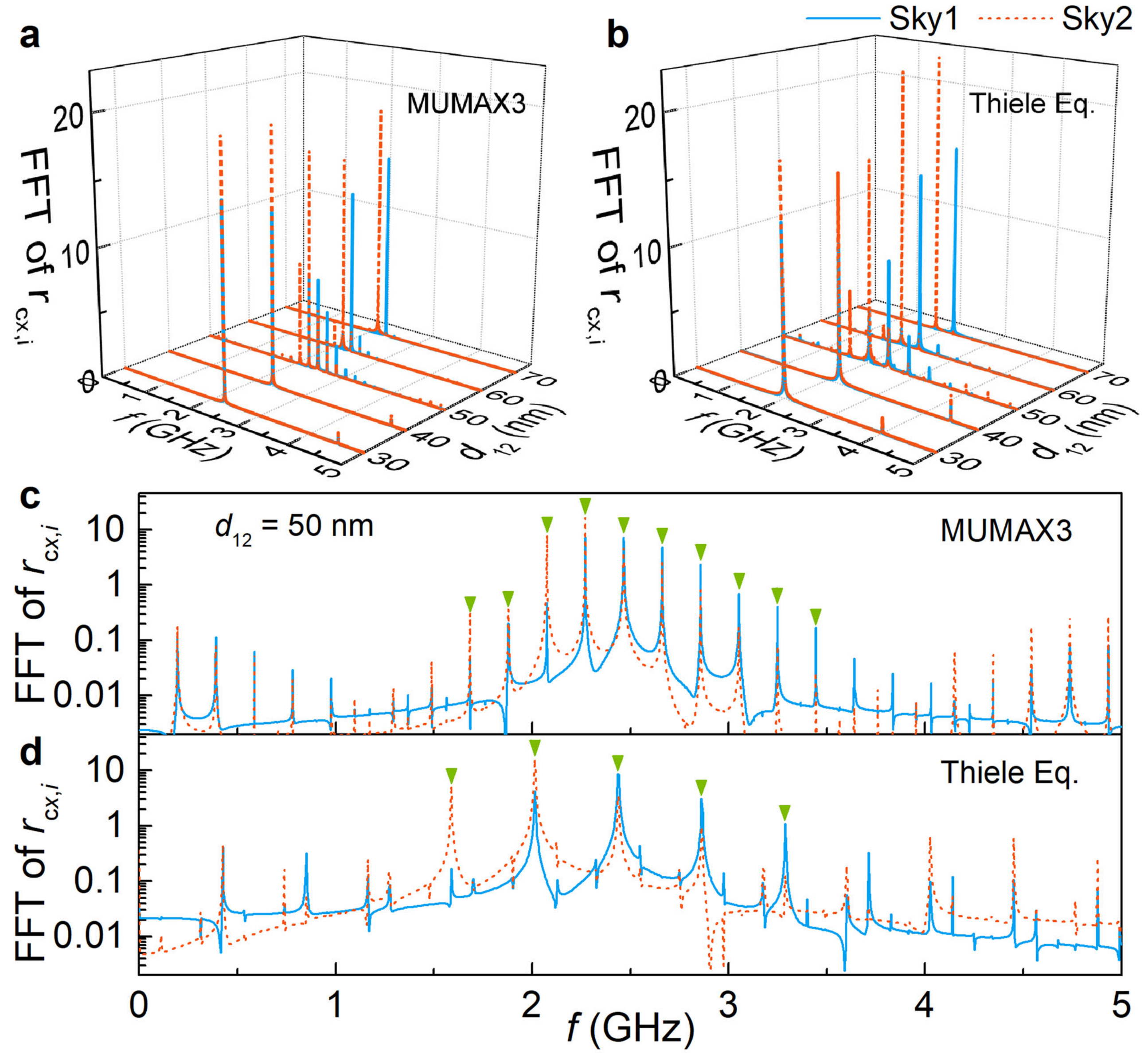

Fig. 2 | Frequency spectra for different oscillator spacings. FFT spectra of $r_{cx,1}$ (blue curve) and $r_{cx,2}$ (orange curve) from **a** MUMAX3 and **b** Thiele' s equation. **c**, **d** Details of frequency spectrum at $d_{12} = 50$ nm. The parameters in this calculation are the same as those used in Fig. 1.

equation nicely reproduce all features obtained from MUMAX3, except a slightly larger difference between the two free-running frequencies, which might be introduced by the approximation in the phenomenological parameters in Thiele's equation. Therefore, our further calculation and analysis on synchronization and frequency comb will be mainly based on the Thiele's equation.

Figure 3a shows the frequencies of the peaks in the FFT of $r_{cx,1}$ and $r_{cx,2}$ as functions of d_{12}. The color of the data points stands for the amplitude of the corresponding FFT peaks. A transition between the synchronization and frequency comb is clearly observed at $d_{12}^* \simeq 41.4$ nm. This behavior is similar to the previous prediction from the classical Kuramoto model[31]. However, after a close comparison with the results of Kuramoto model, we find that the frequencies in Fig. 3a systematically increase when the oscillator spacing approaches d_{12}^* from both sides, whereas those in Kuramoto model are always distributed symmetrically around the average of the two free-running frequencies[55].

To analyze this behavior, we derive the expressions of major frequencies in both synchronization and non-synchronization regions by ignoring the minor inertia term of Eq. (1) (see derivations in Supplementary Note 2), which are found to be in the same form as

$$\omega_i = \frac{\mathbf{F}_{j,i} \cdot \mathbf{e}_{\theta,i}}{\alpha L |\mathbf{r}_{c,i}|}, \tag{2}$$

with $i = 1, 2$ for the two STNOs in the non-synchronization region and i = syn for an effective oscillator after synchronization. For the latter, we define $\mathbf{r}_{c,syn} = \mathbf{r}_{c,1} + \mathbf{r}_{c,2}$ and $\mathbf{F}_{j,syn} = \mathbf{F}_{j,1} + \mathbf{F}_{j,2}$. The unit vector $\mathbf{e}_{\theta,i}$ is along the azimuthal direction perpendicular to $\mathbf{r}_{c,i}$ and L denotes the diagonal component of the dissipative tensor $\mathbf{L}$. In Fig. 3b, c, we present the temporal-averaged values of $r_{c,i}$ and $F_{j\theta,i}$, respectively, as functions of d_{12}, from which we see that $r_{c,i}$ and $F_{j\theta,syn}$ ($F_{j\theta,1}$ and $F_{j\theta,2}$) decrease (increase) in the vicinity of d_{12}^*. The decrease of $F_{j\theta,syn}$ with increasing d_{12} results from the change of the angle between $\mathbf{F}_{j,1}$ and $\mathbf{F}_{j,2}$. By substituting these quantities into Eq. (2), we calculate ω_i and plot them as solid curves in Fig. 3a, which match well with FFT spectrum.

It is noteworthy that in the synchronization region below d_{12}^*, as shown in Supplementary Fig. 3, the relative phase Δ (=$\varphi_1 - \varphi_2$) of the two STNOs displays a small variation around a certain value with time, forming a

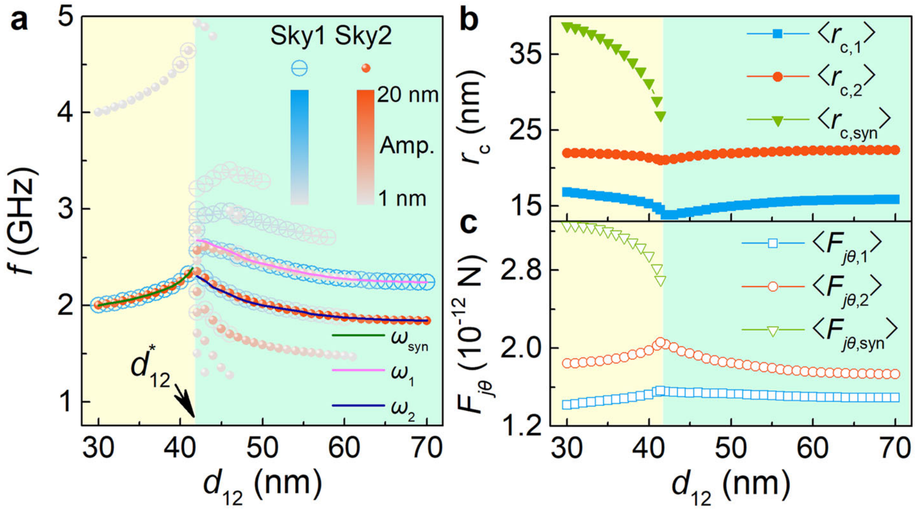

Fig. 3 | Nonmonotonic variation of oscillation frequency with the oscillator spacing. **a** FFT spectra of $r_{cx,1}$ (open symbols) and $r_{cx,2}$ (solid symbols), **b** temporal-averaged orbit radius $r_{c,i}$ and **c** azimuthal component $F_{j\theta,i}$ of current-induced forces, with different oscillator spacings d_{12}. The color bars in **a** represent the amplitude in Fourier transformation. The light yellow and green backgrounds indicate the synchronization and non-synchronization regions, respectively. The curves in **a** are the plots of Eq. (2), while the symbols in **a**–**c** represent the results of the Thiele' s equation with the same parameters as those used in Fig. 1.

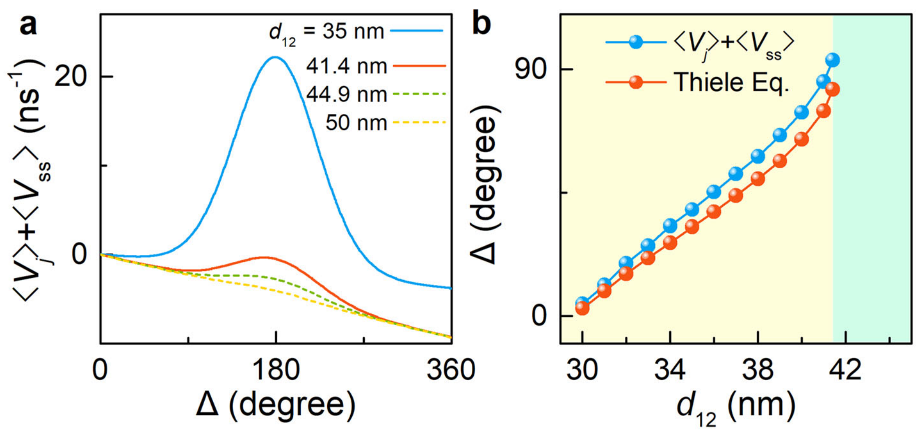

Fig. 4 | Phase difference from effective potentials. **a** The temporal-averaged total effective potential energy as a function of the relative phase between the two oscillators, with different values of d_{12}. **b** The phase difference at the local minimum of the potential energy and that from the Thiele' s equation in the synchronization region. In this calculation, the parameters are the same as those used in Fig. 1.

dancing synchronization[56]. In addition, as seen from Fig. 3a, there is a weak signal at the double synchronization frequency, which is caused by the deviation of the skyrmion trajectory from a perfect circular orbit (see Supplementary Fig. 2b, g)[55,57]. Above d^*_{12}, the relative phase changes over the 2π range (see Supplementary Fig. 3), as expected for a non-synchronization state.

Transition condition from synchronization to frequency comb

The distinct behaviors of the relative phase in synchronization and frequency comb regions inspire us to derive the condition between the two cases from the evolution equation of the relative phase. In practice, we write the evolution equation in the form of two effective potential energies as[58] (see Supplementary Note 2 for the details)

$$\frac{d\Delta}{dt} = -\frac{\partial V_j}{\partial \Delta} - \frac{\partial V_{ss}}{\partial \Delta}, \tag{3}$$

where the effective potential V_j is generated by the current-induced driving forces and can be expressed as

$$V_j = -\left(\frac{F_{j\theta,1}}{\alpha L r_{c,1}} - \frac{F_{j\theta,2}}{\alpha L r_{c,2}}\right)\Delta, \tag{4}$$

depending linearly on Δ. The other potential energy V_{ss} is associated with the skyrmion-skyrmion interaction force, which, under the condition of $r_{c,1} \approx r_{c,2}$ in our simulation, can be approximately described by

$$V_{ss} \approx F\lambda_{ss}\left(\frac{1}{\alpha L r_{c,1}^2} + \frac{1}{\alpha L r_{c,2}^2}\right)e^{\lambda_0 - r_{12}/\lambda_{ss}}, \tag{5}$$

where r_{12} is the distance between the skyrmion centers (see Fig. 1c). The fitting of the numerical results for the interaction potential energy reveals that the three characteristic parameters F, λ_0 and λ_{ss} equal to 2.3×10^{-12} N, 9.68 and 4.348 nm, respectively (see Supplementary Note 1). Equation (5) suggests a higher interacting potential when the skyrmions are close with each other.

In the dancing synchronization region, the relative phase between the two oscillators only shows a small-amplitude vibration around a finite value. The temporal average of Eq. (3) over a period thus gives the vanishing of its left side, leading to $\partial(\langle V_j \rangle + \langle V_{ss} \rangle)/\partial\Delta = 0$. The specific value of the average relative phase $\langle \Delta \rangle$ can be determined from the extremum problem of the total potential energy $\langle V_j \rangle + \langle V_{ss} \rangle$ with respect to Δ. Accordingly, we calculate $\langle V_j \rangle$ and $\langle V_{ss} \rangle$ (see Supplementary Note 2 for the details), and plot $\langle V_j \rangle + \langle V_{ss} \rangle$ as a function of Δ with different values of d_{12} in Fig. 4a. As one can see, for $d_{12} = 35$ nm (far below the critical value $d^*_{12} = 41.4$ nm in Fig. 3), the potential curve has a local minimum value at Δ ~ 39 degrees. As shown in Fig. 4b, the relative phases extracted from this way show reasonable agreement with those based on the Thiele's equation in the whole synchronization region. In the opposite limit with a sufficient large d_{12}, there is

Fig. 5 | Tunability of critical distance. **a** The critical distance d_{12}^{*} as a function of the current density j_1 (with fixed magnetization $M_s^t = 600$ kA m^{-1}) and **b** its dependence on the saturation magnetization M_s^t (with $j_1 = 60$ MA cm^{-2}). The insets show the calculated values of $|\langle V_j \rangle|/\Delta$ with $d_{12} = 40$ nm and 34 nm for **a** and **b**, respectively. Other parameters are the same as those in Fig. 1.

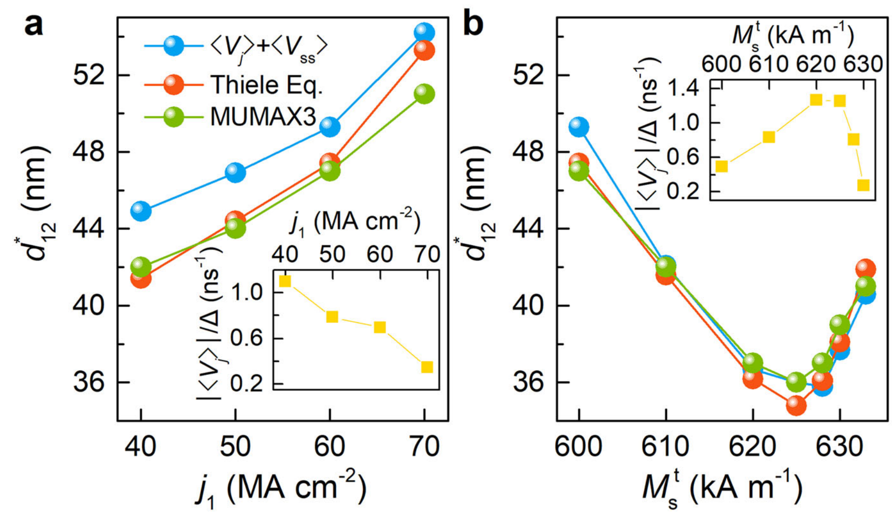

no local minimum in the total potential anymore (see the yellow curve in Fig. 4a with $d_{12} = 50$ nm), reflecting the breakdown of synchronization.

The condition of the synchronization thus corresponds to the appearance of the local minimum point in the Δ dependence of the total potential energy. The potential curve with $d_{12}^{*} = 41.4$ nm, as shown by the red solid curve in Fig. 4a, however, still has a clear local minimum feature. This can be attributed to approximations in the estimation of the potential energy, for example, $r_{c,1} \approx r_{c,2}$. Considering the relatively weak dependence of $\langle V_j \rangle$ on d_{12} and taking its value at $d_{12} = 41.4$ nm, we calculate the total potential with Eq. (5) and find that the local minimum feature starts around $\tilde{d}_{12}^{*} = 44.9$ nm, which is slightly larger than $d_{12}^{*} = 41.4$ nm from the Thiele's equation.

Figure 5a, b summarize the variations of $\tilde{d}_{12}^{*}$, as well as those of d_{12}^{*} from the Thiele's equation and MUMAX3, with the increase of current density j_1 and saturation magnetization M_s^t, respectively. The results from different approaches show nice agreement. The increase of the critical distance in Fig. 5a and the nonmonotonic behavior in Fig. 5b can therefore be understood from the perspective of potential energy. Since the current-induced potential V_j changes linearly with Δ, according to Eq. (4), the formation of the energy minimum state observed in Fig. 4a then relies on the ratio $|V_j|/\Delta$. A larger $|\langle V_j \rangle|/\Delta$ requires a stronger interaction potential $\langle V_{ss} \rangle$ and thus a smaller distance d_{12} to synchronize the two STNOs. For a quantitative estimation, we compute $|\langle V_j \rangle|/\Delta$ from the Thiele's equation for different current densities j_1 (saturation magnetizations M_s^t), as shown in the inset of Fig. 5a (Fig. 5b), where we neglect the weak d_{12}-dependence of $\langle V_j \rangle$ and choose a small oscillator spacing $d_{12} = 40$ nm (34 nm) to ensure the STNOs always in a synchronization state for all adopted parameters. As expected, $|\langle V_j \rangle|/\Delta$ decreases with j_1 and shows a nonmonotonic dependence on M_s^t, explaining well the change of the critical distance. The influences of the damping constant and RKKY coupling coefficient on d_{12}^{*} are summarized in Supplementary Fig. 4. While the critical distance is found to show a nonmonotonic dependence on the RKKY coupling coefficient, it decreases with the increase of damping constant, which can be interpreted by the variation of $\alpha|\langle V_j \rangle|/\Delta$. As shown in Supplementary Fig. 5, the values of $\langle r_{c,i} \rangle$ ($\langle F_{j\theta,i} \rangle$) involved in $|\langle V_j \rangle|$ become smaller (larger) for a higher damping, giving rise to a larger $\alpha|\langle V_j \rangle|/\Delta$ and hence a smaller critical distance.

In contrast to the previous proposals based on dipolar interactions between spatially separated STNOs, the coupling between our SFiM-skyrmion-based STNOs originates mainly from the short-range exchange interactions, while the demagnetization effect of the dipolar interactions is found to play a marginal role (see Supplementary Fig. 6). In addition, the FiM resonance frequency is about 140 GHz for our adopted parameters, which is much higher than the working frequency of our STNOs (about 2 GHz). Thus, the spin-wave excitation and the energy dissipation through it can be neglected in our oscillator system.

Extension to a two-dimensional STNO array

In this section, we take a 3 × 3 STNO array (see Fig. 6a) as an example in our micromagnetic simulation to demonstrate the extension of the foregoing synchronization and frequency comb, as well as their current control, in multiple STNOs with a fixed geometry. In the simulation, we tune the current density of the central STNO (Osc5), j_5, and choose the other driving currents randomly within the range of 65–75 MA cm^{-2} to introduce different working frequencies of the STNOs. Figure 6b shows the FFT spectra of the recorded magnetizations averaged over 45 × 45 nm^2 areas, with different values of j_5. As one can see, the synchronization and frequency comb features do show up for $j_5 = 70$ MA cm^{-2} and $j_5 = 55$ MA cm^{-2}, respectively. Interestingly, for $j_5 = 60$ MA cm^{-2} between them, chaotic peaks appear, implying the loss of the periodicity of skyrmion motion. For a rather smaller current $j_5 = 40$ MA cm^{-2}, on the other hand, we surprisingly find a clear synchronized main frequency accompanying with relatively weak signals at fractional frequencies (1/3 and 2/3 of the main frequency), which might be generated by the strong nonlinearity of the system[59].

The motion of each skyrmion can be read out from the direction of the total magnetization below the corresponding current injection area[60]. In practice, we define the angle between the in-plane magnetization component of the mth STNO and the x axis as θ_m and plot the time evolution of the phase difference between Osc1 and Osc5 in the top panel of Fig. 6c with different values of j_5. We can see that the two oscillators are indeed in synchronization states for $j_5 = 40$ and 70 MA cm^{-2}, but not for $j_5 = 55$ and 60 MA cm^{-2} (see Supplementary Fig. 3 of the two-STNO case). For a full analysis of all STNOs, we compute the order parameter[42],

$$\zeta = \frac{1}{N} \Big| \sum_m e^{i\theta_m} \Big|, \tag{6}$$

where $N = 9$ is the total number of STNOs. As $\zeta = 0$ and 1 correspond to disordered state and perfect synchronization, respectively, the finite value $\zeta > 0.5$, shown in the bottom panel of Fig. 6c, reflects the strong correlation between our STNOs even in the non-synchronization states. The good phase coherence for the synchronization state at $j_5 = 70$ MA cm^{-2} leads to $\zeta \sim 0.92$. It should be pointed out that the choice of the central STNO is essential for the current control, according to Supplementary Fig. 7, where the manipulation of the input currents at Osc1 and Osc2 does not introduce qualitative change in the dynamics. In this work, the thermal effects are not taken into account. One could expect that the trajectories of skyrmions will be affected by the thermal fluctuation, which results in a noisy frequency

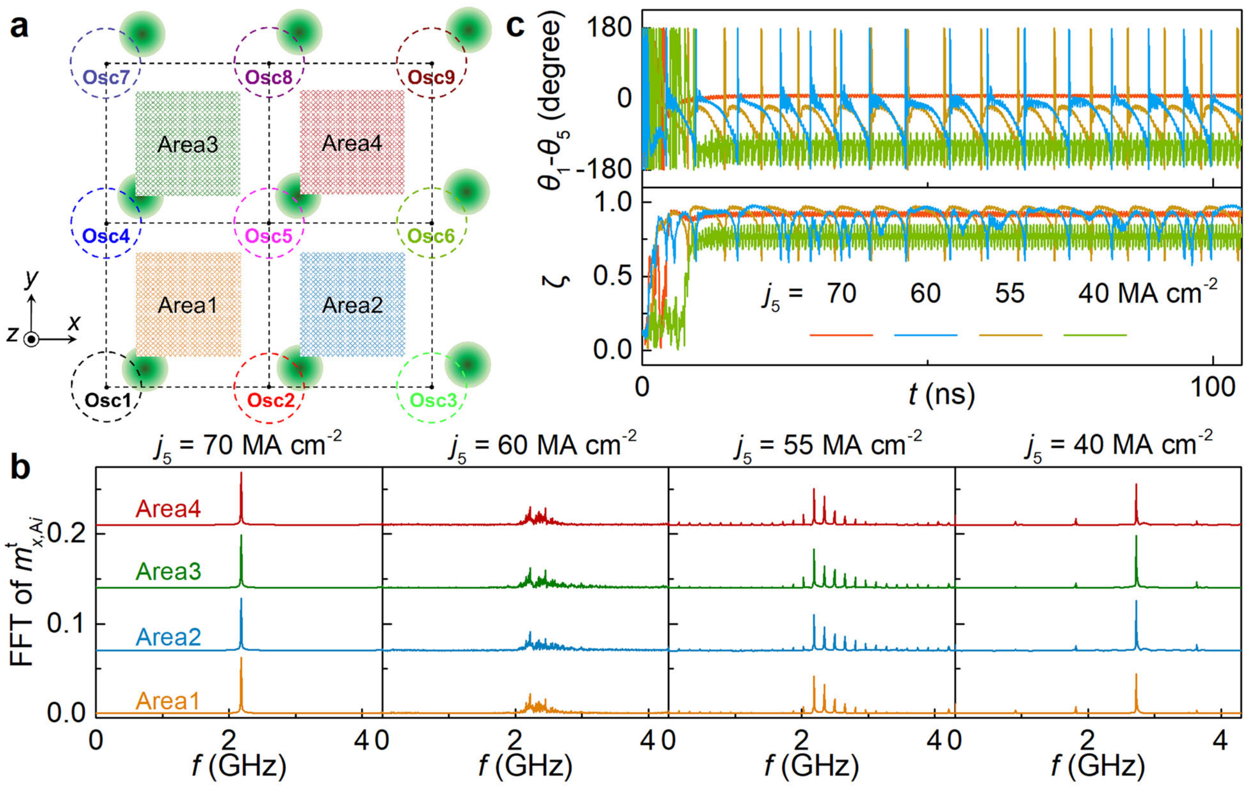

Fig. 6 | Current control in STNO array. a Structure of our 3×3 STNO array under consideration. The dashed circles indicate the current injection areas (labeled Osc1-Osc9) with the identical diameters of 30 nm and center-to-center distance of 70 nm. The current densities are adopted to be 67, 66, 66, 71, 75, 68, 69 and 72 MA cm^{-2} for j_1-j_4 and j_6-j_9. **b** FFT spectra of the recorded magnetizations averaged over 45×45 nm^2 areas, with different values of j_5 injected into the central STNO (Osc5). The curves in **b** have been shifted vertically for clarity. **c** The time evolution of the phase difference $(\theta_1 - \theta_5)$ and order parameter (ζ) with different values of j_5.

spectrum and may prevent the observation of the synchronization and frequency comb at high temperatures. However, such effect could be too weak to play a relevant role at low temperatures, so that the nonlinear dynamical phenomena predicted here should remain identifiable in the frequency spectra.

In conclusion, we investigated the current-induced magnetization dynamics in both coupled FiM-skyrmion-based double STNOs and a multi-STNO array, and found nonlinear dynamical phenomena, including dancing synchronizations and frequency combs. The conditions of the transition between them were systematically calculated through numerical simulations and explicitly analyzed based on the effective potential energies. The switching of different dynamical behaviors by tuning the driving currents was demonstrated.

Methods

Micromagnetic simulations

Micromagnetic simulations of a synthetic ferrimagnet are performed by employing the open-source software MUMAX3[49] to solve the Landau-Lifshitz-Gilbert (LLG) equation[61],

$$\dot{\mathbf{m}}^{\tau} = -\gamma \mathbf{m}^{\tau} \times \mathbf{H}_{\mathrm{eff}}^{\tau} + \alpha \mathbf{m}^{\tau} \times \dot{\mathbf{m}}^{\tau} + \gamma H_j^{\tau} (\mathbf{m}^{\tau} \times \mathbf{p}) \times \mathbf{m}^{\tau}, \qquad (7)$$

where the layer index $\tau = \mathrm{t}$ and b for the top and bottom ferromagnets, respectively. $\mathbf{m}^{\tau}$, γ and α are the reduced magnetization, the gyromagnetic ratio and the damping constant, respectively. $\mathbf{H}_{\mathrm{eff}}^{\tau}$ denotes the effective field,

$$\mathbf{H}_{\mathrm{eff}}^{\mathrm{t(b)}} = \frac{2 J_{\mathrm{RKKY}}}{\mu_0 M_{\mathrm{s}}^{\mathrm{t(b)}} t_z^{\mathrm{t(b)}}} \mathbf{m}^{\mathrm{b(t)}} + \mathbf{H}_{\mathrm{ex}}^{\mathrm{t(b)}} + \mathbf{H}_{\mathrm{DMI}}^{\mathrm{t(b)}} + \mathbf{H}_{\mathrm{an}}^{\mathrm{t(b)}}, \qquad (8)$$

where the four terms on the right side of Eq. (8) represent the RKKY exchange field[47], Heisenberg exchange field, Dzyaloshinskii-Moriya exchange field[62,63] and magneto-crystalline anisotropy field, respectively. J_{RKKY}, μ_0 and M_{s}^{τ} stand for the RKKY coupling coefficient, the vacuum permeability constant and the saturation magnetization, respectively. t_z^{t} (t_z^{b}) is the thickness of the top (bottom) ferromagnet and we set $t_z^{\mathrm{t}} = t_z^{\mathrm{b}} = t_z$. To save computational cost, the effective field does not include the contribution of the demagnetization, mainly resulting in a modification in the skyrmion size, which can be corrected approximately by modulating the Dzyaloshinskii-Moriya interaction (DMI) strength or introducing an effective anisotropy field[64]. H_j^{τ} in Eq. (7) is the strength of dampinglike spin torque, expressed as $H_j^{\tau} = j\hbar P/(2\mu_0 e t_z M_{\mathrm{s}}^{\tau})$ with j being the current density, $\hbar$ the reduced Planck constant, P the spin polarization efficiency and e the elementary charge[65]. The polarization vector $\mathbf{p}$ is set to be along the $-z$ direction.

In our simulations, we take a Co/Pt/Ru/Co/Pt multilayer as the working synthetic ferrimagnet, where the size of each Co layer is $512 \times 512 \times 1$ nm^3 discretized by $1 \times 1 \times 1$ nm^3 unit cells. The material parameters[66] are taken to be the exchange coefficient $A^{\mathrm{t(b)}} = 15$ pJ m^{-1}, the magnetic anisotropy constant $K^{\mathrm{t(b)}} = 0.8$ MJ m^{-3} and the DMI constant $D^{\mathrm{t(b)}} = 4$ mJ m^{-2}. The saturation magnetization $M_{\mathrm{s}}^{\mathrm{b}}$ of the bottom Co layer is fixed to be 580 kA m^{-1}, while $M_{\mathrm{s}}^{\mathrm{t}}$ of the top one is slightly different from $M_{\mathrm{s}}^{\mathrm{b}}$ in order for the magnetizations to exhibit intriguing ferrimagnetic dynamics. Such a difference in the values of M_{s}^{τ} has been experimentally reported in SFiM systems[67]. In addition, we set $P = 0.4$, $\alpha = 0.05$ and $J_{\mathrm{RKKY}} = -1$ mJ m^{-2} (it is experimentally achievable[48]). Note that in our calculations, current-induced spin torques are applied to the local magnetizations of both the top and bottom ferromagnets, so our results of a synthetic ferrimagnet can be directly transferred to a monolayer ferrimagnet.

While the regular (anti)ferromagnet does not allow self-confined skyrmion oscillator in a continuous working layer, both a synthetic ferrimagnet and a single FiM film can be used as the platform for boundary-free skyrmion oscillators[43]. We consider a synthetic ferrimagnet here because of its tunability of RKKY coupling strength via the spacer thickness and the accessibility of the MUMAX3 software for micromagnetic simulations. As an initialization process in magnetic simulations, we start from a homogeneous magnetic state and apply a relatively strong current (with the intensity of 600 MA cm^{-2} and duration of 1.16 ns) into the current injector (Fig. 1a) to generate one SFiM skyrmion in each oscillator. The simulation results are presented in Supplementary Fig. 8.

Data availability

The data supporting the findings of this study are available within this article and its Supplementary Information. Additional data that support the findings of this study are available from the corresponding author on reasonable requests.

Code availability

The micromagnetic simulation software MUMAX3 used in this work is open-source and can be accessed freely at http://mumax.github.io/.

Received: 8 August 2023; Accepted: 26 February 2024;
Published online: 08 March 2024

References

1. Kaka, S. et al. Mutual phase-locking of microwave spin torque nano-oscillators. *Nature* **437**, 389–392 (2005).
2. Ruotolo, A. et al. Phase-locking of magnetic vortices mediated by antivortices. *Nat. Nanotechnol.* **4**, 528–532 (2009).
3. Dussaux, A. et al. Large microwave generation from current-driven magnetic vortex oscillators in magnetic tunnel junctions. *Nat. Commun.* **1**, 8 (2010).
4. Hamadeh, A. et al. Origin of Spectral Purity and Tuning Sensitivity in a Spin Transfer Vortex Nano-Oscillator. *Phys. Rev. Lett.* **112**, 257201 (2014).
5. Khvalkovskiy, A. V., Grollier, J., Dussaux, A., Zvezdin, K. A. & Cros, V. Vortex oscillations induced by spin-polarized current in a magnetic nanopillar: Analytical versus micromagnetic calculations. *Phys. Rev. B* **80**, 140401 (2009).
6. Liang, X., Shen, L., Xing, X. & Zhou, Y. Elongated skyrmion as spin torque nano-oscillator and magnonic waveguide. *Commun. Phys.* **5**, 310 (2022).
7. Zhang, S. et al. Current-induced magnetic skyrmions oscillator. *N. J. Phys.* **17**, 023061 (2015).
8. Zeng, Z., Finocchio, G. & Jiang, H. Spin transfer nano-oscillators. *Nanoscale* **5**, 2219 (2013).
9. Imai, Y., Tsunegi, S., Nakajima, K. & Taniguchi, T. Noise-induced synchronization of spin-torque oscillators. *Phys. Rev. B* **105**, 224407 (2022).
10. Urazhdin, S., Tabor, P., Tiberkevich, V. & Slavin, A. Fractional Synchronization of Spin-Torque Nano-Oscillators. *Phys. Rev. Lett.* **105**, 104101 (2010).
11. Jiang, S. et al. Field-Free High-Frequency Exchange-Spring Spin-Torque Nano-Oscillators. *Nano Lett.* **23**, 1159–1166 (2023).
12. Slonczewski, J. Current-driven excitation of magnetic multilayers. *J. Magn. Magn. Mater.* **159**, L1–L7 (1996).
13. Berger, L. Emission of spin waves by a magnetic multilayer traversed by a current. *Phys. Rev. B* **54**, 9353–9358 (1996).
14. Rippard, W., Pufall, M., Kaka, S., Russek, S. & Silva, T. Direct-Current Induced Dynamics in $Co_{90}Fe_{10}/Ni_{80}Fe_{20}$ Point Contacts. *Phys. Rev. Lett.* **92**, 027201 (2004).
15. Mancoff, F. B., Rizzo, N. D., Engel, B. N. & Tehrani, S. Phase-locking in double-point-contact spin-transfer devices. *Nature* **437**, 393–395 (2005).
16. Zahedinejad, M. et al. Two-dimensional mutually synchronized spin Hall nano-oscillator arrays for neuromorphic computing. *Nat. Nanotechnol.* **15**, 47–52 (2020).
17. Vogel, A. et al. Coupled Vortex Oscillations in Spatially Separated Permalloy Squares. *Phys. Rev. Lett.* **106**, 137201 (2011).
18. Pribiag, V. S. et al. Magnetic vortex oscillator driven by d.c. spin-polarized current. *Nat. Phys.* **3**, 498–503 (2007).
19. Lebrun, R. et al. Mutual synchronization of spin torque nano-oscillators through a long-range and tunable electrical coupling scheme. *Nat. Commun.* **8**, 15825 (2017).
20. Martins, L. et al. Second harmonic injection locking of coupled spin torque vortex oscillators with an individual phase access. *Commun. Phys.* **6**, 72 (2023).
21. Garcia-Sanchez, F., Sampaio, J., Reyren, N., Cros, V. & Kim, J.-V. A skyrmion-based spin-torque nano-oscillator. *N. J. Phys.* **18**, 075011 (2016).
22. Shen, L. et al. Spin torque nano-oscillators based on antiferromagnetic skyrmions. *Appl. Phys. Lett.* **114**, 042402 (2019).
23. Jin, C. et al. Array of Synchronized Nano-Oscillators Based on Repulsion between Domain Wall and Skyrmion. *Phys. Rev. Appl.* **9**, 044007 (2018).
24. Romera, M. et al. Vowel recognition with four coupled spin-torque nano-oscillators. *Nature* **563**, 230–234 (2018).
25. Romera, M. et al. Binding events through the mutual synchronization of spintronic nano-neurons. *Nat. Commun.* **13**, 883 (2022).
26. Kanao, T. et al. Reservoir Computing on Spin-Torque Oscillator Array. *Phys. Rev. Appl.* **12**, 024052 (2019).
27. Grollier, J., Querlioz, D. & Stiles, M. D. Spintronic Nanodevices for Bioinspired Computing. *Proc. IEEE* **104**, 2024–2039 (2016).
28. Grollier, J. et al. Neuromorphic spintronics. *Nat. Electron.* **3**, 360–370 (2020).
29. Torrejon, J. et al. Neuromorphic computing with nanoscale spintronic oscillators. *Nature* **547**, 428–431 (2017).
30. Grollier, J., Cros, V. & Fert, A. Synchronization of spin-transfer oscillators driven by stimulated microwave currents. *Phys. Rev. B* **73**, 060409 (2006).
31. Kuramoto, Y. Self-entrainment of a population of coupled non-linear oscillators. In *International Symposium on Mathematical Problems in Theoretical Physics* 420–422 (Springer, 1975).
32. Del'Haye, P. et al. Optical frequency comb generation from a monolithic microresonator. *Nature* **450**, 1214–1217 (2007).
33. Cundiff, S. T. & Ye, J. *Colloquium*: Femtosecond optical frequency combs. *Rev. Mod. Phys.* **75**, 325–342 (2003).
34. Fortier, T. & Baumann, E. 20 years of developments in optical frequency comb technology and applications. *Commun. Phys.* **2**, 153 (2019).
35. Chang, L., Liu, S. & Bowers, J. E. Integrated optical frequency comb technologies. *Nat. Photon.* **16**, 95–108 (2022).
36. Kendziorczyk, T., Demokritov, S. O. & Kuhn, T. Spin-wave-mediated mutual synchronization of spin-torque nano-oscillators: A micromagnetic study of multistable phase locking. *Phys. Rev. B* **90**, 054414 (2014).
37. Berkov, D. V. Synchronization of spin-torque-driven nano-oscillators for point contacts on a quasi-one-dimensional nanowire: Micromagnetic simulations. *Phys. Rev. B* **87**, 014406 (2013).
38. Kendziorczyk, T. & Kuhn, T. Mutual synchronization of nanoconstriction-based spin Hall nano-oscillators through evanescent and propagating spin waves. *Phys. Rev. B* **93**, 134413 (2016).
39. Erokhin, S. & Berkov, D. Robust synchronization of an arbitrary number of spin-torque-driven vortex nano-oscillators. *Phys. Rev. B* **89**, 144421 (2014).
40. Wang, Z. et al. Magnonic Frequency Comb through Nonlinear Magnon-Skyrmion Scattering. *Phys. Rev. Lett.* **127**, 037202 (2021).
41. Wang, Z., Yuan, H., Cao, Y. & Yan, P. Twisted Magnon Frequency Comb and Penrose Superradiance. *Phys. Rev. Lett.* **129**, 107203 (2022).

42. Flovik, V., Maciá, F. & Wahlström, E. Describing synchronization and topological excitations in arrays of magnetic spin torque oscillators through the Kuramoto model. *Sci. Rep.* **6**, 32528 (2016).
43. Shen, L., Zhou, Y. & Shen, K. Boundary-free spin torque nano-oscillators based on ferrimagnetic skyrmions. *Appl. Phys. Lett.* **121**, 092403 (2022).
44. Brearton, R., van der Laan, G. & Hesjedal, T. Magnetic skyrmion interactions in the micromagnetic framework. *Phys. Rev. B* **101**, 134422 (2020).
45. Wang, Y., Wang, J., Kitamura, T., Hirakata, H. & Shimada, T. Exponential Temperature Effects on Skyrmion-Skyrmion Interaction. *Phys. Rev. Appl.* **18**, 044024 (2022).
46. Wang, X.-G. et al. Skyrmion Echo in a System of Interacting Skyrmions. *Phys. Rev. Lett.* **129**, 126101 (2022).
47. Parkin, S. S. P., Bhadra, R. & Roche, K. P. Oscillatory magnetic exchange coupling through thin copper layers. *Phys. Rev. Lett.* **66**, 2152–2155 (1991).
48. Saito, Y., Ikeda, S. & Endoh, T. Synthetic antiferromagnetic layer based on Pt/Ru/Pt spacer layer with 1.05 nm interlayer exchange oscillation period for spin-orbit torque devices. *Appl. Phys. Lett.* **119**, 142401 (2021).
49. Vansteenkiste, A. et al. The design and verification of MuMax3. *AIP Adv.* **4**, 107133 (2014).
50. Thiele, A. A. Steady-State Motion of Magnetic Domains. *Phys. Rev. Lett.* **30**, 230–233 (1973).
51. Kim, S. K., Lee, K.-J. & Tserkovnyak, Y. Self-focusing skyrmion racetracks in ferrimagnets. *Phys. Rev. B* **95**, 140404(R) (2017).
52. Shen, L. et al. Nonreciprocal dynamics of ferrimagnetic bimerons. *Phys. Rev. B* **105**, 014422 (2022).
53. Barker, J. & Tretiakov, O. A. Static and Dynamical Properties of Antiferromagnetic Skyrmions in the Presence of Applied Current and Temperature. *Phys. Rev. Lett.* **116**, 147203 (2016).
54. Komineas, S. & Papanicolaou, N. Skyrmion dynamics in chiral ferromagnets. *Phys. Rev. B* **92**, 064412 (2015).
55. Wood, C. J. & Camley, R. E. Synchronization of oscillators arising from second-order, and higher, nonlinear couplings. *Nonlinear Dyn.* **108**, 597–611 (2022).
56. Wu, H. T., Wang, L., Min, T. & Wang, X. R. Dancing synchronization in coupled spin-torque nano-oscillators. *Phys. Rev. B* **104**, 014305 (2021).
57. Yoo, M.-W. et al. Pattern generation and symbolic dynamics in a nanocontact vortex oscillator. *Nat. Commun.* **11**, 601 (2020).
58. Chen, H.-H. et al. Phase locking of spin-torque nano-oscillator pairs with magnetic dipolar coupling. *Phys. Rev. B* **93**, 224410 (2016).
59. Shen, L. et al. Current-Induced Dynamics and Chaos of Antiferromagnetic Bimerons. *Phys. Rev. Lett.* **124**, 037202 (2020).
60. Kang, W., Huang, Y., Zhang, X., Zhou, Y. & Zhao, W. Skyrmion-Electronics: An Overview and Outlook. *Proc. IEEE* **104**, 2040–2061 (2016).
61. Gilbert, T. A Phenomenological Theory of Damping in Ferromagnetic Materials. *IEEE Trans. Magn.* **40**, 3443–3449 (2004).
62. Dzyaloshinsky, I. A thermodynamic theory of "weak" ferromagnetism of antiferromagnetics. *J. Phys. Chem. Solids* **4**, 241–255 (1958).
63. Moriya, T. Anisotropic Superexchange Interaction and Weak Ferromagnetism. *Phys. Rev.* **120**, 91–98 (1960).
64. Rohart, S. & Thiaville, A. Skyrmion confinement in ultrathin film nanostructures in the presence of Dzyaloshinskii-Moriya interaction. *Phys. Rev. B* **88**, 184422 (2013).
65. Shen, L., Zhou, Y. & Shen, K. Programmable skyrmion-based logic gates in a single nanotrack. *Phys. Rev. B* **107**, 054437 (2023).
66. Sampaio, J., Cros, V., Rohart, S., Thiaville, A. & Fert, A. Nucleation, stability and current-induced motion of isolated magnetic skyrmions in nanostructures. *Nat. Nanotechnol.* **8**, 839–844 (2013).
67. Jang, S. Y., You, C.-Y., Lim, S. H. & Lee, S. R. Annealing effects on the magnetic dead layer and saturation magnetization in unit structures relevant to a synthetic ferrimagnetic free structure. *J. Appl. Phys.* **109**, 013901 (2011).

Acknowledgements
This work is supported by the National Natural Science Foundation of China (Grants No. 11974047 and No. 12374100) and the Fundamental Research Funds for the Central Universities.

Author contributions
K.S. coordinated the project. L.S. and L.Q. performed the numerical simulations and theoretical calculations. L.S. and K.S. wrote the manuscript with useful comments from L.Q. L.S. and L.Q. contributed equally to this work.

Competing interests
The authors declare no competing interests.

Additional information
Supplementary information The online version contains supplementary material available at https://doi.org/10.1038/s41524-024-01233-6.

Correspondence and requests for materials should be addressed to Ka Shen.